









## RESEARCH ARTICLE

10.1029/2021JA029675

# MESSENGER X-Ray Observations of Electron Precipitation on the Dayside of Mercury

S. T. Lindsay<sup>1</sup> , E. J. Bunce<sup>1</sup> , S. M. Imber<sup>1,2</sup> , A. Martindale<sup>1</sup> , L. R. Nittler<sup>3</sup> , and T. K. Yeoman<sup>1</sup> 

<sup>1</sup>University of Leicester, School of Physics & Astronomy, Leicester, UK, <sup>2</sup>Department of Atmospheric, Oceanic and Space Sciences, University of Michigan, Ann Arbor, MI, USA, <sup>3</sup>Department of Terrestrial Magnetism, Carnegie Institute of Washington, Washington, DC, USA

### Key Points:

- We have isolated electron-induced X-ray fluorescence on the dayside of Mercury to a confidence level dependent on solar X-ray flux
- The areas of X-ray emission show where electrons reach the surface, and clarify the interaction between Mercury's magnetosphere and surface
- Instead of identifying specific events as solar- or electron-induced, we gradually relax a solar filter to see the changes in precipitation

### Supporting Information:

Supporting Information may be found in the online version of this article.

### Correspondence to:

S. T. Lindsay,  
s.t.lindsay@le.ac.uk

### Citation:

Lindsay, S. T., Bunce, E. J., Imber, S. M., Martindale, A., Nittler, L. R., & Yeoman, T. K. (2022). MESSENGER X-ray observations of electron precipitation on the dayside of Mercury. *Journal of Geophysical Research: Space Physics*, 127, e2021JA029675. <https://doi.org/10.1029/2021JA029675>

Received 27 JUL 2021  
Accepted 20 DEC 2021

### Author Contributions:

**Conceptualization:** S. T. Lindsay, E. J. Bunce, S. M. Imber, A. Martindale, L. R. Nittler, T. K. Yeoman  
**Data curation:** S. T. Lindsay, L. R. Nittler  
**Formal analysis:** S. T. Lindsay  
**Funding acquisition:** E. J. Bunce  
**Investigation:** S. T. Lindsay, E. J. Bunce, S. M. Imber  
**Methodology:** S. T. Lindsay, A. Martindale, L. R. Nittler  
**Project Administration:** E. J. Bunce  
**Software:** S. T. Lindsay, A. Martindale  
**Supervision:** E. J. Bunce

**Abstract** The first maps of electron-induced X-ray emission from the dayside of Mercury's surface are presented, generated by the development of a solar X-ray flux filter. This enables the isolation of the X-ray fluorescence of calcium driven by probable electron precipitation. A catalog of such events has been generated and dayside maps of implied electron precipitation zones have been produced. We find that, similar to electron induced emission events on the nightside, these zones are strongly organized by latitude and magnetic local time. The majority of the dayside events appear in the southern hemisphere and there is a strong enhancement observed centered about local dawn (06:00 LT). There is apparent poleward continuation of emission in the north, but very few events were observed on the duskward hemisphere. These results carry implications for Mercury's magnetosphere by constraining zones of electron precipitation, for the exosphere as a potential source of exospheric species, and for surface science as an additional source of X-ray fluorescence.

**Plain Language Summary** Mercury has a magnetic field which is similar to Earth's, and charged particles (electrons and protons) within it move in similar ways. At Earth, particles which reach the atmosphere generate the aurora borealis and aurora australis (northern and southern lights). At Mercury, there is no atmosphere so these particles reach the surface, where they produce X-rays. At night, it is relatively simple to detect these X-rays and map the regions where they are being produced, because the only source of X-rays is the particles reaching the surface. During the day, however, the signal can easily be overwhelmed because at the same time X-rays are being produced in response to illumination by the Sun. We have been able to tentatively isolate the X-ray signal coming from charged particles during the day on Mercury by applying a filter which takes into account the brightness of the Sun in X-rays at the same time. When the sun is dim in X-rays but the surface is bright, we can be confident that the surface signal comes from charged particles, and vice versa.

## 1. Introduction

NASA's Mercury Surface, Space Environment, Geochemistry and Ranging (MESSENGER; Solomon et al., 2007) probe was launched on 3 August 2004 and inserted into orbit about Mercury on 18 March 2011. The cruise phase involved six planetary gravity assist maneuvers, three of which involved Mercury. After an extremely successful, twice-extended four-year mission, producing many ground-breaking results (see for example Solomon et al., 2018), the probe was de-orbited and impacted the planetary surface on 30 April 2015.

In order to study the planet's magnetosphere as well as its surface, MESSENGER's orbit was highly elliptical and near-polar, with a periapsis altitude of 200–500 km over the northern pole and an apoapsis of 15,000 or 10,000 km (before and after an orbit adjustment on 20 April 2012) above the southern hemisphere. The orbit plane was fixed with respect to the line of apsides of the Mercury orbit, and as such the planet rotated underneath the spacecraft approximately every 118 spacecraft orbits (McAdams et al., 2007) - one Mercury sidereal day - providing global coverage.

The X-Ray Spectrometer, XRS (Schlemm et al., 2007), was part of the MESSENGER surface geochemistry suite of instruments. It was a gas proportional counter-based X-ray fluorescence spectrometer with a 12° hexagonal field of view, using three cylinders (GPCs 1, 2 and 3) filled with an Ar/CH<sub>4</sub> mixture, two of which (GPCs 1 and 2) were equipped with elemental filters to allow separation of the Mg/Al/Si peaks in the range 1.2–1.8 keV. XRS was paired with the Solar Assembly for X-rays (SAX), a Si PIN diode operating as a solar X-ray monitor. SAX was mounted in the spacecraft sunshield and as such was always pointing within 12° of the spacecraft-Sun

© 2022. The Authors.

This is an open access article under the terms of the [Creative Commons Attribution License](https://creativecommons.org/licenses/by/4.0/), which permits use, distribution and reproduction in any medium, provided the original work is properly cited.

**Validation:** S. T. Lindsay  
**Visualization:** S. T. Lindsay, L. R. Nittler  
**Writing – original draft:** S. T. Lindsay  
**Writing – review & editing:** E. J. Bunce, S. M. Imber, A. Martindale, L. R. Nittler, T. K. Yeoman

line due to mission pointing constraints (McAdams et al., 2007). Both XRS and SAX had energy resolutions of  $\sim 900$  eV FWHM at the Fe-K line (Schlemm et al., 2007).

XRS was designed to detect X-ray fluorescence from the surface of the planet, driven by illumination by solar coronal X-rays. However, early results from MESSENGER's orbital mission included the detection of fluorescent X-rays from the nightside surface of the planet (Starr et al., 2012), where solar X-ray flux evidently cannot be the illuminating source. Instead, charged particle precipitation at the surface, likely to be electrons, was identified as the probable source. Data from MESSENGER's first flyby of Mercury had already provided strong evidence for the presence of 1–10 keV electrons in the planet's magnetosphere (Ho et al., 2011; Slavin et al., 2008). (Korth et al., 2014) discussed the north-south asymmetry in plasma distribution due to the northward offset of the planetary dipole.

Lindsay et al. (2016) showed that the sites of this electron precipitation, as inferred by the detection of X-ray fluorescence events from the unlit surface of the planet where no solar signal is present, are strongly asymmetric in local time, with many more events occurring downward of local midnight than towards dusk. The emission is also organized in latitude, with two latitudinal bands appearing mirrored about the magnetic equator and with a poleward limit co-located with the open-closed field line boundary according to the KT15 model (Korth et al., 2015). The precipitation of electrons in such “auroral” zones was predicted from Mariner 10 data by Baker et al. (1987), and the potential of these zones as a source of X-rays by Grande (1997), although both overestimated the strength of the effect due to the high energy particle fluxes observed by Mariner 10 (Simpson et al., 1974), which may have been mischaracterized as a result of instrumental pileup (Armstrong et al., 1975).

To date, our studies of electron-induced X-ray fluorescence have eliminated solar photon induced X-ray fluorescence events by the simple method of only considering events detected when the entirety of the XRS footprint on the surface of Mercury is in darkness. However, there is no obvious magnetospheric/exospheric mechanism which would restrict electron precipitation to the unlit hemisphere; indeed, the local time distribution shown in Figure 2 of Lindsay et al. (2016) indicates that it is likely that precipitation continues onto the dayside of Mercury. Here, therefore, we present a new filtering method allowing for the first time the identification of electron-induced fluorescence events on the sunlit surface of the planet with a level of confidence which is higher when the level of solar illumination is lower. We then apply this method to produce maps of electron precipitation sites extending to the dayside of Mercury in order to help understand the complex coupling between the magnetosphere/exosphere and the surface, and also to determine the location and frequency of electron precipitation.

## 2. Materials and Methods

A catalog of dayside electron-induced X-ray fluorescence events was constructed using two stages of filtering; the first filter was used to identify XRS records containing the fluorescence of Si and Ca planetwide irrespective of illumination, and the second filter acted to categorize this catalog according to the simultaneous solar illumination. These filters were then used to characterize dayside electron-induced X-ray fluorescence zones according to the corresponding level of solar illumination.

### 2.1. Identification of Fluorescence Events

Catalogs of all fluorescence events (an “event” consists of an individual XRS record, which range from 20 to 500 s in integration time) were constructed for fluorescence from the planetary surface using a peak-fitting algorithm, covering the full MESSENGER orbital mission from March 2011 to April 2015. One catalog was generated for fluorescence at the Si-K $\alpha$  line, and a second (a subset of the first) for fluorescence at the Ca-K $\alpha$  line. The algorithm was similar to that used to generate the catalogs described in (Lindsay et al., 2016) with the exception that here events are not rejected if the instrument footprint was illuminated (partly or fully) by the Sun. In step 7 below the filter rejects records which show evidence of instrumental self-fluorescence driven by in situ energetic particles (Ho et al., 2011); during these events, count rates at the fluorescence energies of the elements composing the instrumental filters (Al and Mg) are elevated above the count rate at the same energies in the unfiltered detector. In step 8, the filter rejects records where the instrument's footprint is off planet, to exclude X-rays from astrophysical sources in the field of view (Bannister et al., 2012). Other than these two steps, the filter does not attempt to differentiate records on the basis of the origin of the fluorescence event.

The filter is used by applying criteria to each XRS calibrated data record (CDR) as follows. The filter:

1. Rejects records with a low integrated count rate ( $<2 \text{ s}^{-1}$  over whole spectrum)
2. Uses a peak finder (Dimeo, 2004) to check that there are more than zero count rate peaks in the GPC energy spectrum. If no peaks are found, record is rejected
3. Attempts a least-squares fit of a Gaussian curve to the GPC3 (i.e., the unfiltered GPC) energy spectrum with a peak centered at 1.74 keV (Si-K $\alpha$ )
4. If the fitted peak has a maximum in the range  $1.5 < E < 1.95$  keV, a width in the range  $0.9 < \text{FWHM} < 1.4$  keV, and a coefficient of determination  $R^2 > 0.8$  (all criteria are selected empirically), then the record is flagged as containing Si fluorescence
5. If the record is flagged, the filter fits a peak to the GPC3 energy spectrum at 3.69 keV (Ca-K $\alpha$ )
6. If the fitted peak has a maximum in the range  $3.4 < E < 3.8$  keV, a width in the range  $1.4 < \text{FWHM} < 1.8$  keV, and a coefficient of determination  $R^2 > 0.9$  (all criteria are selected empirically by adjusting parameters until the data set produced by the automated filter closely matches one selected manually), then the record is flagged as containing Ca fluorescence
7. If instrumental self-fluorescence is observed in the Mg and Al filters (i.e., Mg/Al count rate at Mg/Al-filtered GPCs is elevated above Mg/Al count rate at unfiltered GPC), the record is rejected for both Si and Ca fluorescence
8. If the telemetry point (given by XRS CDR telemetry) indicates that the instrument footprint is pointing partially or entirely off planet, the record is rejected for both Si and Ca fluorescence. This is done to reject observations of astrophysical X-ray sources, such as those described in Bannister et al. (2012)

Note that step 5 necessarily implies that the Ca fluorescence catalog is a subset of the Si fluorescence catalog, because fitting to the Ca peak is only conducted if fitting to the Si peak has succeeded. We consider this a reasonable limitation as Ca fluorescence is not expected to be observed without simultaneous Si fluorescence; all sources of illumination for X-ray fluorescence (solar or particle) can be expected to be more intense at the Si-K $\alpha$  line than at the Ca-K $\alpha$  line, and Si is present in significantly higher quantities on the surface.

The catalogs produced by this method contain 120,000 and 6,600 events for Si and Ca fluorescence respectively; this is significantly larger than our previously reported catalogs since dayside events are not excluded. The critical development over and above this catalog arises from the development of a more refined secondary filter that was applied to allow categorization of these catalogs into solar-driven and particle-driven events. This method relies upon the simultaneously recorded solar X-ray flux spectrum from SAX as follows.

## 2.2. Rejection of Solar-Driven Events

Having constructed an all-planet catalog of surface fluorescence in Si and Ca, we now need to reject spectra showing enhanced Si and Ca which are driven by intervals of high activity on the Sun. In doing so, we are able to extract those data which are most likely to have been driven dominantly, or entirely, by particle precipitation to the surface.

Figure 1 shows typical solar-induced surface X-ray spectra from XRS (panels d, e and f) observed during variable levels of solar flux. The simultaneously observed solar X-ray spectra from SAX are shown in panels a, b and c. The shaded areas on panels a, b and c show solar X-ray flux with sufficient energy to drive fluorescence in Si (both shaded areas) and Ca (dark shading only). These are X-rays with energies above the Si and Ca K-absorption edges; that is, the minimum energy required to generate the initial electron vacancy that leads to emission of a fluorescent X-ray. Any particle or X-ray with an energy above this value absorbed by the target material has the potential to cause X-ray fluorescence. Dashed lines on panels e and f show the expected center of the Ca fluorescence peak, if observed.

Note that the Ca peak is only resolvable at high flare states (Figure 1 panels c and f, and weakly in panels b and e), while the Si peak is resolvable during much lower levels of solar activity (Figure 1 panels a and d).

Each XRS event in the Si and Ca fluorescence catalogs was compared with the solar flux observed at the same observation time by SAX, integrated over energies at or above 1.84 keV and 4.04 keV respectively (i.e., the light and dark gray areas shaded in Figure 1 a, b and c), corresponding to the Si and Ca K-edges.

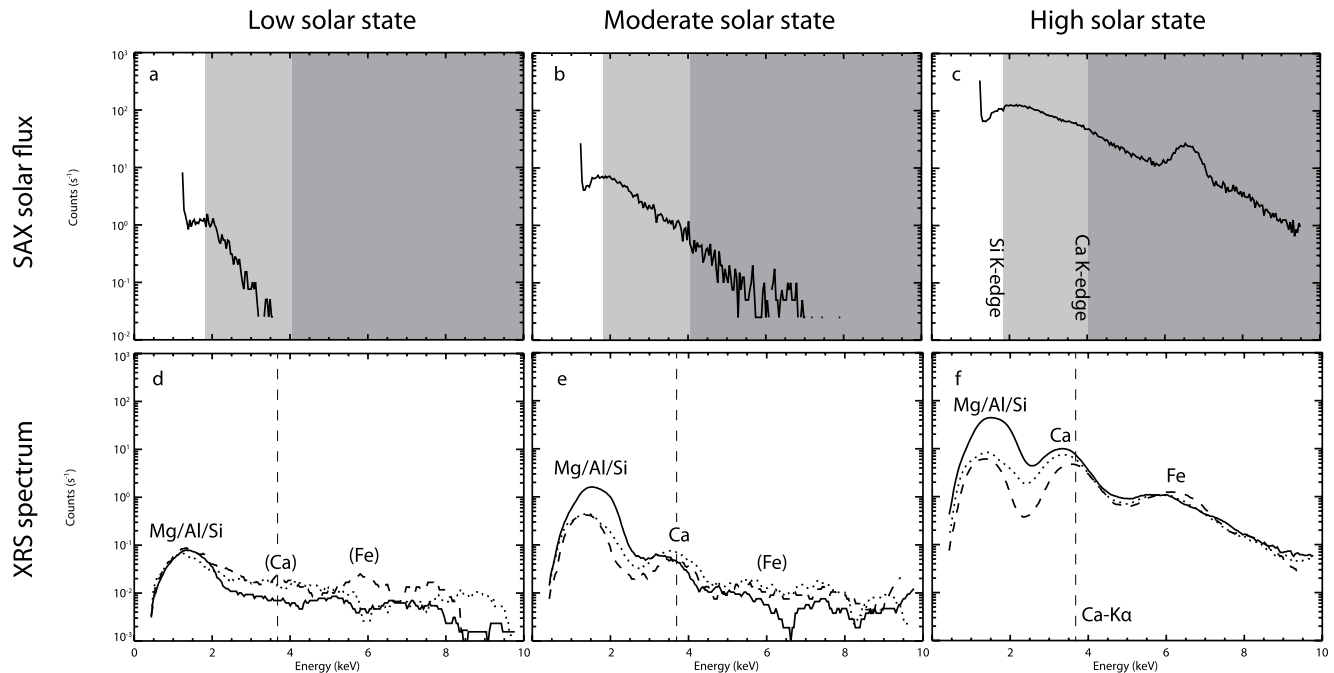


**Figure 1.** Example solar and surface X-ray spectra, selected as representative of various levels of solar X-ray flux and typical surface response. Solar Assembly for X-rays (a,b,c) and X-ray Spectrometer (d–f) spectra at (a–d) 01:21:25 UTC on 18 October 2013 (b–e) 09:00:10 UTC on 21 July 2013 and (c–f) 00:48:10 UTC on 10 May 2013 with flux above Si K-edge (light gray) and above Ca K-edge (dark gray) shaded and Ca-K $\alpha$  fluorescence line highlighted. Location of elemental fluorescence peaks is identified (in parentheses where no peak is visible).

A thresholding process was then introduced, such that (Si or Ca) X-ray fluorescence events are only included in a catalog of potentially particle-induced events if the solar X-ray flux, integrated for all energies above the relevant (Si or Ca) absorption edge, is below a certain threshold level. This threshold level was varied from zero (i.e., events were only included in the catalog if no flux at all was seen above the relevant absorption edge) to  $10^3 \text{ s}^{-1}$  in  $\log_{10}$  intervals of 0.025. In effect, this process searches for events where a surface spectrum resembling Figure 1e or 1f is observed while the simultaneous solar spectrum is similar to Figure 1a. The highest count rate produces a catalog very similar to the pre-thresholding catalog, as integrated flux rarely exceeds such a high value and thus almost all levels of solar flux are permitted.

This process was repeated using a slightly different thresholding based on the ratio between two channel ranges in the SAX spectrum as a proxy for solar temperature (channels 45–55:channels 75–85, after Weider et al. (2015)) rather than absolute flux above a certain level. The hardness of the solar X-ray spectrum varies closely with total flux, so a similar result was expected from this alternative method.

The maps generated by using this ratio are very similar to the results described below, and are included in the Supporting Information S3 and S4.

In the limit of low solar flux (low values of the applied threshold), any significant X-ray emission is attributed to the same electron precipitation which has previously been observed only on the nightside surface (Lindsay et al., 2016; Starr et al., 2012). In the limit of high solar flux (large values of the applied threshold) emission from the sunlit surface is dominated by X-rays stimulated by solar-coronal X-rays. The following section describes an iterative procedure to determine which events can be confidently attributed to electron precipitation on the sunlit hemisphere in order to identify the locations associated with significant X-ray emission via non-solar stimulus.

Variation of the threshold level between these two extremes should result in a transition from electron-dominated to solar-dominated fluorescence events in the associated catalogs. Given that the catalog covers a period of time during which the MESSENGER orbit precesses about the planet approximately 32 times, surface coverage is effectively complete and solar-induced events should be expected to be distributed evenly across the sunlit surface (assuming an even distribution of the fluorescing elements across the surface), while the spatial distribution of electron-induced events on the dayside is not yet known.

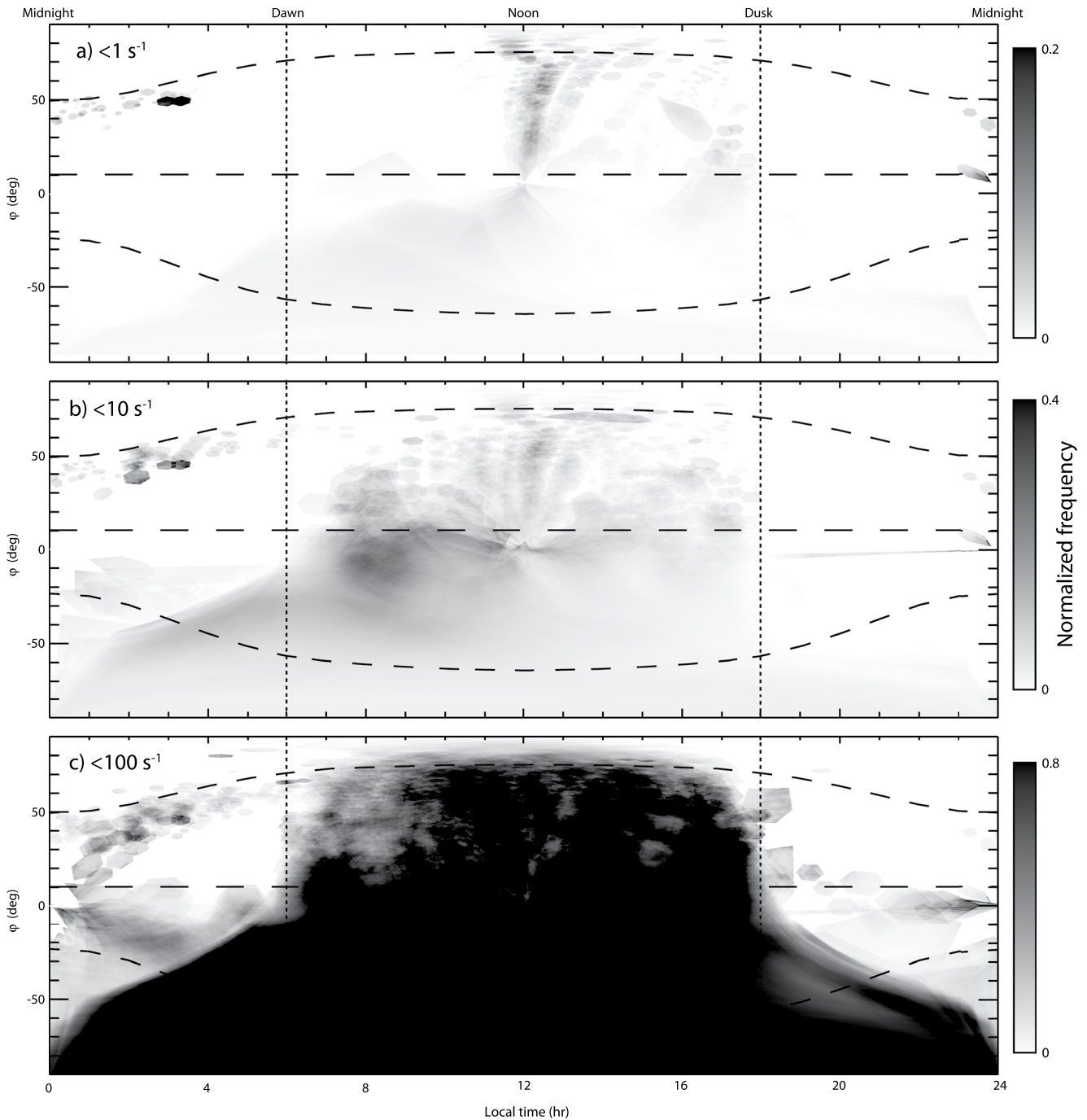


**Figure 2.** Maps in local time and latitude of XRS footprint locations containing electron-induced Si surface fluorescence with records with SAX integrated count rates above 1.84 keV of at least (a)  $1 \text{ s}^{-1}$ , (b)  $10 \text{ s}^{-1}$  and (c)  $100 \text{ s}^{-1}$  filtered out; dashed lines represent the magnetic equator and the average open-closed field line boundary per Korth et al. (2015). Color bar shows fraction of total available observation time in which fluorescence is observed and not rejected by the filter, in accordance with the viewing assumptions discussed in the text.

### 3. Results

Figure 2 shows three panels of maps in latitude and local time of the XRS surface footprints of all Si fluorescence events not excluded by the filters described above, with records with simultaneous SAX count rates, integrated for all energies above the Si K-edge, above low ( $1 \text{ s}^{-1}$ , top panel), medium ( $10 \text{ s}^{-1}$ , middle panel) and high ( $100 \text{ s}^{-1}$ , bottom panel) thresholds filtered out. Animations showing the change of surface footprint patterns as



the threshold increases at  $\log_{10}$  intervals of 0.025 are available in the Supporting Information S1. The greyscale index shows the cumulative integration time where fluorescence (which is not excluded by the filter) is observed from footprints covering the relevant area, normalized by the total integration time in which the instrument was observing the same area over the whole duration of the mission. Note that this quantity necessarily assumes that the full footprint is fluorescing; as XRS is a collimating instrument we are not able to determine whether this is the case or, if it is not, what proportion of the footprint is emitting X-rays. In particular, intensities in the southern hemisphere are likely to be underestimates since the larger footprints mean that the likelihood the entire footprint is indeed fluorescing is lower. Likewise, we have no information of duration of fluorescence events on timescales shorter than the integration time of individual records and must assume that fluorescence continues for the full duration of each record.

When the threshold is relaxed to  $100 \text{ s}^{-1}$  (Figure 2c), and both electron and solar-driven fluorescence is expected, event distribution across the dayside hemisphere (as well as near the south pole, where footprints are very large and are almost always at least partially lit) becomes near-isotropic. This is expected behavior, as with a high flux threshold a large number of solar-induced Si fluorescence events are included, which should be evenly distributed across the sunlit surface. At lower thresholds of  $1 \text{ s}^{-1}$  and  $10 \text{ s}^{-1}$  (Figures 2a and 2b respectively), there are not enough events to produce complete coverage of the dayside, but the distributions observed show evidence of solar-induced (and evenly-distributed) fluorescence events—these are expected and are the result of weak enhancements in solar X-ray flux and spectral hardness. Even at the lowest threshold (top panel) most events occur in individual swath patterns, which are indicative of flare-like events increasing solar X-ray flux over short timescales, causing a string of XRS records over a single orbit to exhibit strong fluorescence.

On the nightside the open-closed field line boundary-aligned precipitation patterns as described in Lindsay et al. (2016), are still visible. Note that the southern group only appears when the solar flux threshold is relaxed (moved to higher values), despite the non-solar origin of this group. We believe this to be a result of the spacecraft being much more likely to be eclipsed by Mercury when above the northern hemisphere, and thus more likely to record lower levels of solar flux as the sun will not be within the SAX FOV. As a result of MESSENGER's elliptical orbit, SAX is likely to have the Sun in its field of view while XRS is viewing the nightside southern hemisphere, and therefore these records are filtered in the same manner as dayside records even though the XRS FOV is unlit.

We do not expect electron precipitation to occur isotropically over the planetary surface, and our previous observations indicate that the patterns associated with the open-closed field line boundary should remain relatively stable, at least on the length scale of XRS footprints. A possible exception is the “extreme cusp” scenario described by Slavin et al. (2014), where some areas of the planetary surface may be exposed directly to the solar wind. In this scenario, the cusps are expected to move equatorward and merge. This is expected to be rare and be correlated with high levels of solar activity, and hence solar X-ray photon flux onto the surface, although the increase in particle energy and density would be expected to be significantly delayed relative to the increase in X-ray photon flux given the relative travel times of solar X-rays and charged particles.

Therefore, we interpret this uniform distribution at all solar flux thresholds as an indication that, because of the dominance of solar-induced fluorescence, electron- and solar-induced Si fluorescence events cannot be isolated from one another on the dayside by this method for any level of solar X-ray flux encountered throughout the MESSENGER mission; the solar flux is always high enough during precipitation events to mask the precipitating electron signatures.

Figure 3 shows similar maps of the footprints of events in the Ca fluorescence catalog, using an identical format for the low, medium and high solar activity thresholds. Animations showing the change of surface footprint patterns as the threshold increases at  $\log_{10}$  intervals of 0.025 are available in the Supporting Information S2. Besides the nightside OCB-aligned regions of precipitation, the most persistent feature is a region of frequent fluorescence in the southern hemisphere, centered around local dawn. This enhancement appears to be a continuation of the southern nightside latitudinal band. It is the strongest feature observed on the dayside when solar X-ray flux is low (Figure 3a), with no organized continuation in the southern hemisphere beyond this dawn enhancement. In the north, the latitudinal band of precipitation observed on the nightside continues for some two hours noonward of the terminator, while continuing to move poleward, following the average dayside OCB.

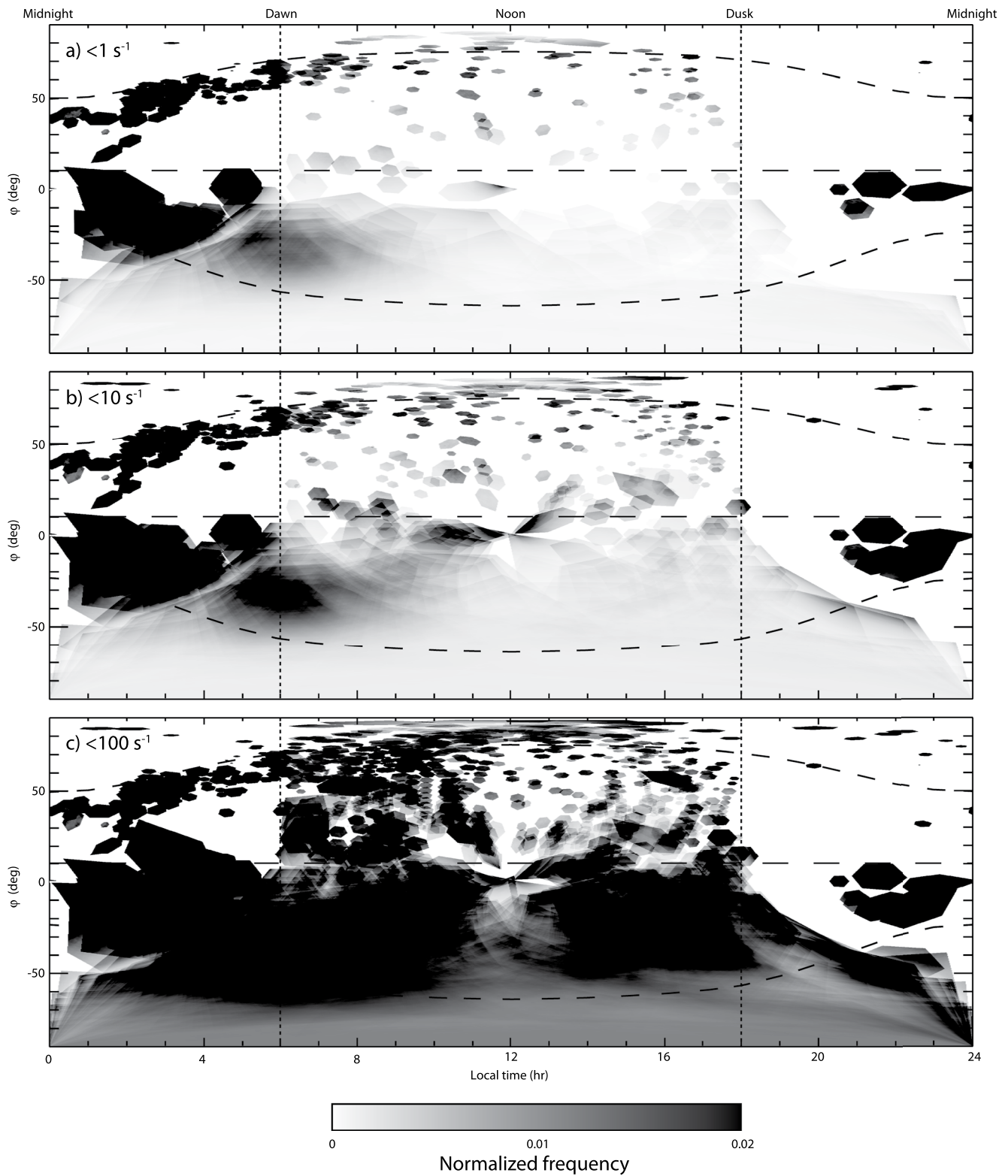


**Figure 3.** Maps in local time and latitude of XRS footprint locations containing electron-induced Ca surface fluorescence with records with SAX integrated count rates above 4.04 keV of (a)  $1 \text{ s}^{-1}$ , (b)  $10 \text{ s}^{-1}$  and (c)  $100 \text{ s}^{-1}$  filtered out; dashed lines represent the magnetic equator and the average open-closed field line boundary per Korth et al. (2015); dotted lines show the terminator. Color bar shows proportion of total available observation time in which fluorescence is observed and not rejected by the filter, in accordance with the viewing assumptions discussed in the text.

Compared to the Si fluorescence maps in Figure 2, the maps of Ca fluorescence evolve in a manner much closer to that expected if we observe mostly electron-induced events at low solar flux and mostly solar-induced events at high flux. When the threshold is very low (Figure 3a), events on the dayside are strongly organized by local time, with an area of relatively frequent X-ray production appearing south of the equator at dawn.

At higher values of solar flux, event locations tend towards the expected uniform distribution associated with fluorescence caused by solar X-rays. In Figure 3c, which includes events correlated with SAX count rates of up to  $100 \text{ s}^{-1}$ , organized features are overwhelmed by an isotropic distribution of events whose edges are well defined by the terminator (dotted vertical lines) in the northern hemisphere.

Mercury has a 3:2 spin:orbit resonance in its orbit about the Sun, meaning that two Mercury years are the same duration as three Mercury days. Together with this, MESSENGER's orbit and its precession about the planet once each Mercury day will mean that the instrument observes certain combinations of longitude and local time much more often than others (see Supporting Information S1 for a heat map of the longitude/local time mapping pairs most frequent in the MESSENGER data set). Therefore the local time associated with any one footprint is not strictly independent of the longitude of that footprint, and a longitudinal (i.e., geographic) region of increased Ca abundance could in theory explain an apparent increase in the local time distribution of Ca fluorescence. However, no such enhancement has been identified from the XRS data (Nittler et al., 2020; Solomon et al., 2018). Figure 4 shows the Ca fluorescence data set plotted as in Figure 3b, along with the same data set plotted in latitude-longitude space and a Ca/Si ratio map adapted from Nittler et al. (2020).

MESSENGER's observations of the system can be considered in terms of both a surface-fixed geographical coordinate system (where a particular region of the surface is fluorescing, regardless of its location in magnetic local time) and magnetic coordinates (where a point relative to the larger Sun-Mercury system is fluorescing). If a portion of the surface was continually fluorescing, this would appear as two stripes in the magnetic coordinate system (due to the resonances in the system discussed above). Conversely, if the fluorescence is observed at a single magnetic local time, this enhancement would be observed as two patches of emission at different longitudes in the surface-fixed geographic coordinate system. The top panel of Figure 4 highlights a region (dashed oval) of emission in magnetic coordinates. In the second panel, two regions of emission are observed and are likewise highlighted with dashed ovals. Due to the resonance, any one feature in latitude-local time would be expected to map to two in latitude-longitude and vice versa. Thus, the observation of a single feature in latitude-local time and two in latitude-longitude strongly suggests that the emission is fixed in magnetic coordinates, and is not due to geographical surface features. Furthermore, no enhancement in Ca abundance is observed in the highlighted regions (bottom panel), which would be necessary to explain a geographical origin for these enhancements.

It is also possible that a real enhancement in local time could be exaggerated by coincidental Ca enhancements in either or both of the corresponding regions in longitude, but no such enhancement appears in the highlighted regions in Figure 4c. Indeed, a significant enhancement in Ca is seen southeast of the easternmost of the projected regions without a corresponding enhancement in particle-driven Ca fluorescence in either longitude or local time. In the southern hemisphere, XRS resolution makes it difficult to definitively exclude the influence of localized regions of elevated Ca abundance, and we must await higher resolution mapping from BepiColombo MIXS.

#### 4. Discussion

The results described here expand upon and clarify the behavior of electrons in the Mercury magnetosphere, including most notably a strong dawn-dusk asymmetry, previously described by (Lindsay et al., 2016) and others (Baker et al., 2015; Ho et al., 2016; Lawrence et al., 2015; Schriver et al., 2011a; Starr et al., 2012). As seen in Figure 3, nightside precipitation of electrons is observed in latitudinal bands which are symmetrical about the magnetic equator, and with a poleward boundary imposed by the (modeled) open-closed field line boundary. As these emission distributions pass the terminator to the dayside, the northern enhancement continues noonward and poleward past the terminator before apparently disappearing at a local time of approximately 8h, while in the south a second region of emission forms, approximately centered at local dawn and a latitude of  $\sim 40^\circ\text{S}$ . As in the north, the distribution does not continue at any significant level further towards noon past approximately 8h local time. No significant enhancements in precipitation are seen on the dusk side of the planet towards either the nightside or the dayside – confirming that the dawn-dusk asymmetry noted in Lindsay et al. (2016) is not a selection effect.



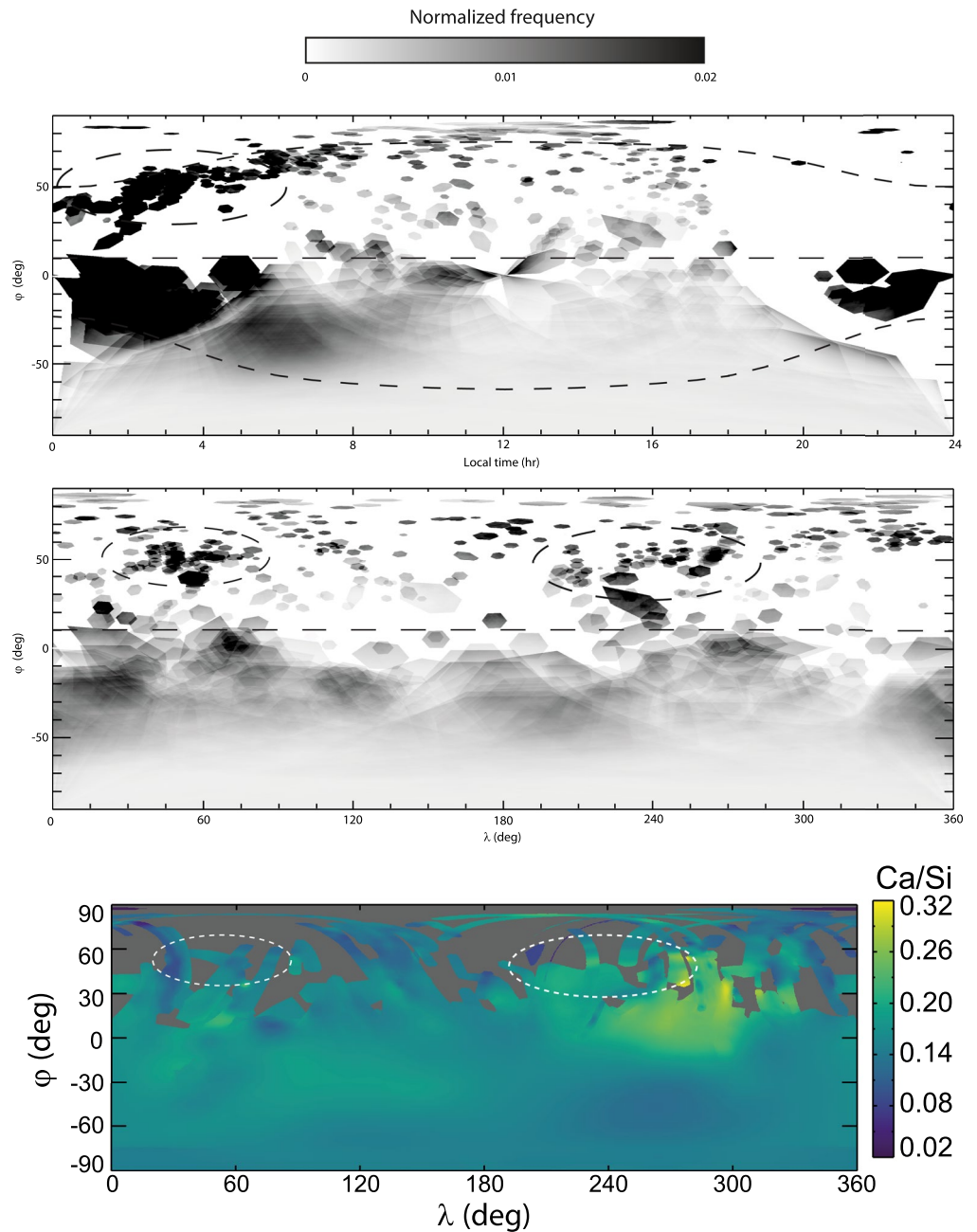


**Figure 4.** (top) Map in local time and latitude of XRS footprint locations containing electron-induced Ca surface fluorescence with records with a SAX integrated count rate above  $10 \text{ s}^{-1}$  (middle) the same event footprint catalog plotted in latitude-longitude space. Approximate areas of the northern enhancement in precipitation in local time and its two counterparts in longitude are highlighted (bottom) Ca/Si ratio map from XRS data, adapted from Nittler et al. (2020), with the same areas highlighted.

Note that there is a pronounced north-south asymmetry in the size of instrument footprints since the spacecraft is much further from the planet when below the equator, and the effect of this on the apparent relative extents of the areas of precipitation in the north and south is not easily separated from any real north-south asymmetry in the signal from Mercury. As discussed in (Lindsay et al., 2016) on the nightside, a north-south asymmetry exists in the apparent size of the regions of precipitation; these results show that this asymmetry continues to the dayside of the planet, and while the larger size of footprints in the south is difficult to separate from real asymmetries, averaging over time is likely to somewhat lessen this effect.

The presence of such an area of enhanced electron precipitation has implications for magnetospheric, exospheric and surface science, each of which is discussed briefly below.

#### 4.1. Magnetosphere

Electrons within the magnetosphere moving from the nightside towards the dayside drift preferentially towards dawn. At least part of this population precipitates onto the nightside surface, largely within two latitudinal bands. The detection of areas of frequent electron precipitation at dawn without continuation past  $\sim 8$ h LT suggests that a large fraction of these drifting electrons may be lost within a relatively small range of local times. These observations support the particle motion modeled by Walsh et al. (2014), who predict latitudinal groupings of precipitation. The model also predicts a significantly larger southern loss cone and thus would predict larger precipitation regions in the southern hemisphere than in the north, however this may also be explained by the north-south asymmetry in the instrument field of view, and these two effects cannot be disentangled using only the data from XRS. Walsh et al. (2014) do not report the longitudinal distribution of precipitating particles, and we cannot make any direct inferences about particle energy (beyond the  $>4$  keV energy required to fluoresce Ca) or trajectory from the locations of precipitation; further investigation of particle motion is therefore beyond the scope of this paper.

Under normal conditions, we do not expect solar wind particles to precipitate directly onto the dayside surface of the planet. Under extreme solar wind conditions, it is possible that the increased ram pressure on the sunward magnetopause, coupled with high dayside reconnection rates, allows direct precipitation of the solar wind onto the dayside surface of the planet, which may be more likely to be in the south due to the weaker dipole (Heyner et al., 2016; Slavin et al., 2018). However, the increased solar wind conditions will be accompanied by greatly increased solar X-ray emission, making identification of these events difficult or impossible by the methods described here. Case-by-case investigation of known incidences of extreme solar-wind conditions may yield better results than the more synoptic view described in this paper.

#### 4.2. Exosphere

We note that an equatorial “dawn source” of exospheric species exists and is correlated with micrometeoritic impact vaporization as a result of Mercury’s motion through the interplanetary dust disk (Burger et al., 2014). This source exhibits some seasonal variation, which has been attributed to the yearly enhancement in micrometeoroid density encountered by Mercury as it passes through the tail of Comet Encke (Killen & Hahn, 2015). While the results reported here show that significant electron precipitation also occurs at dawn, we do not believe it likely to be a dominant component of this dawn source and/or its variability, as it is centered in both north and south at mid-to high-latitudes, without any significant component extending towards the equator. However, electron precipitation can still be expected to produce some exo-ionospheric species ( $\text{Na}^+$ ,  $\text{O}^+$ ,  $\text{H}^+$ ) via electron-stimulated desorption (ESD) resulting from these accelerated electrons; an analysis would be worthwhile but is beyond the scope of this paper. Order of magnitude estimates of ESD intensity from Domingue et al. (2014) based on precipitation rate estimates from Schriver et al. (2011b) and laboratory ESD measurements suggest ion production rates planetwide of  $\sim 10^{23} \text{ s}^{-1}$ . While this is coincidentally comparable to the production rate for Ca neutrals in the dawn source ( $10^{23} \text{ s}^{-1}$ ) measured by Burger et al. (2014), this is not a like-for-like comparison and the production rate of neutrals by ESD is likely to be much lower. Precipitating electrons could plausibly slightly enhance the production of ions in spatially organized regions, and joint observations (Milillo et al., 2020) between Bepi-Colombo’s suite of exospheric instruments (PHEBUS (Quémerais et al., 2020), SERENA (Orsini et al., 2021), MSASI (Yoshikawa et al., 2010)) as well as XRS’ counterpart MIXS (Bunce et al., 2020), are needed to be able to separate any contribution from ESD.

#### 4.3. Surface

X-ray fluorescence analysis of the planetary surface in regions that may experience electron precipitation simultaneously with solar X-ray illumination must take into account the possibility that some of the emission is electron-induced. Characterizing the location and frequency of emission relative to surface-fixed geographical coordinates will assist in removal of contamination of the solar-induced signal by electron-induced fluorescence in the records, and enable the solar-photon generated fluorescence to be identified. The energy, spatial and

time resolution of the equivalent instrument onboard BepiColombo, the Mercury Imaging X-ray Spectrometer (MIXS), is much higher, so electron precipitation and the resultant contribution to the fluorescent signal must be properly understood and taken into account when analyzing MIXS data, since a localized competing source of fluorescence may otherwise lead to incorrect calculation of relative surface elemental abundances. The fact that it is difficult to conclusively demonstrate that locations of events in our Si catalog are organized by the magnetic field implies that under most conditions the solar induced flux on the dayside is dominant at low energy. Future MIXS data pertaining to the major rock-forming elements Mg, Al and Si, the primary observable for MIXS, will not be significantly affected, but more care may be needed in analyzing data for higher energy species such as Ca.

It is possible that the precipitation of charged particles to the surface could change the chemical composition of the surface over extremely long timescales, in a manner similar to that observed at the polar caps of Ganymede (Khurana et al., 2007). If the regions of precipitation described here have been stable over very long ( $10^6$  years or longer) periods, loss rates of the magnitudes described by Domingue et al. (2014) could result in changes in the bulk composition of the surface. Whether such changes have occurred, or whether the effect is discernible against a background of effects with significantly higher ion production rates (sputtering, thermal desorption) is an open question.

## 5. Conclusions

We have developed the first two-stage filter to isolate fluorescence events on the surface of Mercury and then to determine the differences in distribution between solar-induced and particle-induced fluorescence events. These filters indicate that there is a significant enhancement in the occurrence of Ca fluorescence, located at local dawn and in the northern and southern hemispheres, which is not attributable to solar illumination. We attribute these enhancements to the precipitation of electrons injected into the nightside magnetosphere which drift downward before reaching the surface.

These results extend our map of locations of surface precipitation to cover the whole planet, add constraints for future modeling of particle motion within Mercury's magnetosphere, and pave the way for further studies by BepiColombo. One of the primary science objectives of BepiColombo MIXS (Bunce et al., 2020) is to “confirm that the auroral zone, where energetic particles interact with the surface, is an intense source of continuum and line X-rays.” MIXS will be able to expand on the findings described here in significant ways: its improved spatial resolution and imaging capability will allow improved characterization of the locations where electron precipitation drives X-ray emission; its larger energy range will allow the detection of X-rays at lower energies, and thus the better characterization of the illuminating electron spectrum and potential detection of additional precipitation events at lower energies; while the BepiColombo MPO orbit will allow for observations in the Southern hemisphere at the same altitudes and thus resolutions as in the North. The existence of dayside electron precipitation, and the method for its isolation outlined in this paper, will significantly enhance science possibilities for MIXS and BepiColombo.

## Data Availability Statement

This work made use of the MESSENGER E/V/H XRS CALIBRATED (CDR) SPECTRA v1.0 data set (Starr, 2010) archived by the NASA Planetary Data System at the PDS Geosciences Node, Washington University, St Louis, MO, USA. This work used the ALICE High Performance Computing Facility at the University of Leicester.

## Acknowledgments

This work is supported by STFC Science Activities Grant ST/S002596/1. EJB and TKY are supported by STFC Consolidated Grant ST/N000749/1. EJB is supported by a Royal Society Wolfson Research Merit Award. This work was funded by UK Space Agency grant numbers ST/P000908/1, ST/T001542/1, ST/K003194/1, ST/L000318/1, ST/M000702/1.

## References

- Armstrong, T. P., Krimigis, S. M., & Lanzerotti, L. J. (1975). A reinterpretation of the reported energetic particle fluxes in the vicinity of Mercury. *Journal of Geophysical Research*, 80(28), 4015–4017. <https://doi.org/10.1029/JA080i028p04015>
- Baker, D. N., Borovsky, J. E., Burns, J. O., Gislis, G. R., & Zeilik, M. (1987). Possible calorimetric effects at mercury due to solar wind-magnetosphere interactions. *Journal of Geophysical Research*, 92(A5), 4707–4712. <https://doi.org/10.1029/JA092iA05p04707>
- Baker, D. N., Dewey, R., Anderson, B. J., Ho, G., Korth, H., Krimigis, S., et al. (2015). Energetic electron flux enhancements in Mercury's magnetosphere: An integrated view with multi-instrument observations from Messenger. *Geophysical Research Abstracts*, 17, 2517.
- Bannister, N. P., Fraser, G. W., Lindsay, S. T., Martindale, A., & Talboys, D. L. (2012). Astrophysical objects observed by the MESSENGER X-ray spectrometer during Mercury flybys. *Planetary and Space Science*, 69, 28–39. <https://doi.org/10.1016/j.pss.2012.05.006>

- Bunce, E. J., Martindale, A., Lindsay, S., Muinonen, K., Rothery, D. A., Pearson, J., et al. (2020). The BepiColombo mercury imaging X-ray spectrometer: Science goals, instrument performance and operations. *Space Science Reviews*, 216(8), 126. <https://doi.org/10.1007/s11214-020-00750-2>
- Burger, M. H., Killen, R. M., McClintock, W. E., Merkel, A. W., Vervack, R. J., Jr, Cassidy, T. A., & Sarantos, M. (2014). Seasonal variations in Mercury's dayside calcium exosphere. *Icarus*, 238, 51–58. <https://doi.org/10.1016/j.icarus.2014.04.049>
- Dimeo, R. M. (2004). In *get\_peak\_pos.pro* NIST center for neutron research. NIST Center for Neutron Research.
- Domingue, D. L., Chapman, C. R., Killen, R. M., Zurbuchen, T. H., Gilbert, J. A., Sarantos, M., et al. (2014). Mercury's weather-Beaten surface: Understanding mercury in the context of lunar and asteroidal space weathering studies. *Space Science Reviews*, 181(1), 121–214. <https://doi.org/10.1007/s11214-014-0039-5>
- Grande, M. (1997). Investigation of magnetospheric interactions with the Hermean surface. *Advances in Space Research*, 19(10), 1609–1614. [https://doi.org/10.1016/S0273-1177\(97\)00374-8](https://doi.org/10.1016/S0273-1177(97)00374-8)
- Heyner, D., Nabert, C., Liebert, E., & Glassmeier, K.-H. (2016). Concerning reconnection-induction balance at the magnetopause of Mercury. *Journal of Geophysical Research: Space Physics*, 121(4), 2935–2961. <https://doi.org/10.1002/2015JA021484>
- Ho, G. C., Starr, R. D., Gold, R. E., Krimigis, S. M., Slavin, J. A., Baker, D. N., et al. (2011). Observations of suprathermal electrons in Mercury's magnetosphere during the three MESSENGER flybys. *Planetary and Space Science*, 59, 2016–2025. <https://doi.org/10.1016/j.pss.2011.01.011>
- Ho, G. C., Starr, R. D., Krimigis, S. M., Vandegriff, J. D., Baker, D. N., Gold, R. E., et al. (2016). MESSENGER observations of suprathermal electrons in Mercury's magnetosphere. *Geophysical Research Letters*, 43(2), 550–555. <https://doi.org/10.1002/2015GL066850>
- Khurana, K. K., Pappalardo, R. T., Murphy, N., & Denk, T. (2007). The origin of Ganymede's polar caps. *Icarus*, 191(1), 193–202. <https://doi.org/10.1016/j.icarus.2007.04.022>
- Killen, R. M., & Hahn, J. M. (2015). Impact vaporization as a possible source of Mercury's calcium exosphere. *Icarus*, 250, 230–237. <https://doi.org/10.1016/j.icarus.2014.11.035>
- Korth, H., Anderson, B. J., Gershman, D. J., Raines, J. M., Slavin, J. A., Zurbuchen, T. H., et al. (2014). Plasma distribution in Mercury's magnetosphere derived from MESSENGER magnetometer and fast imaging plasma spectrometer observations. *Journal of Geophysical Research: Space Physics*, 119, 2917–2932. <https://doi.org/10.1002/2013ja019567>
- Korth, H., Tsyganenko, N. A., Johnson, C. L., Philpott, L. C., Anderson, B. J., Al Asad, M. M., et al. (2015). Modular model for Mercury's magnetospheric magnetic field confined within the average observed magnetopause. *Journal of Geophysical Research: Space Physics*, 120(6), 4503–4518. <https://doi.org/10.1002/2015JA021022>
- Lawrence, D. J., Anderson, B. J., Baker, D. N., Feldman, W. C., Ho, G. C., Korth, H., et al. (2015). Comprehensive survey of energetic electron events in Mercury's magnetosphere with data from the MESSENGER Gamma-Ray and Neutron Spectrometer. *Journal of Geophysical Research: Space Physics*, 120(4), 2851–2876. <https://doi.org/10.1002/2014JA020792>
- Lindsay, S. T., James, M. K., Bunce, E. J., Imber, S. M., Korth, H., Martindale, A., & Yeoman, T. K. (2016). MESSENGER X-ray observations of magnetosphere-surface interaction on the nightside of Mercury. *Planetary and Space Science*, 125, 72–79. <https://doi.org/10.1016/j.pss.2016.03.005>
- McAdams, J. V., Farquhar, R. W., Taylor, A. H., & Williams, B. G. (2007). MESSENGER mission design and navigation. *Space Science Reviews*, 131(1–4), 219–246. <https://doi.org/10.1007/s11214-007-9162-x>
- Milillo, A., Fujimoto, M., Murakami, G., Benkhoff, J., Zender, J., Aizawa, S., et al. (2020). Investigating Mercury's environment with the two-spacecraft BepiColombo mission. *Space Science Reviews*, 216(5), 93. <https://doi.org/10.1007/s11214-020-00712-8>
- Nittler, L. R., Frank, E. A., Weider, S. Z., Crapster-Pregont, E., Vorburger, A., Starr, R. D., & Solomon, S. C. (2020). Global major-element maps of Mercury from four years of MESSENGER X-Ray Spectrometer observations. *Icarus*, 345, 113716. <https://doi.org/10.1016/j.icarus.2020.113716>
- Orsini, S., Livi, S. A., Lichtenegger, H., Barabash, S., Milillo, A., De Angelis, E., et al. (2021). Serena: Particle instrument suite for determining the sun-mercury interaction from BepiColombo. *Space Science Reviews*, 217(1), 11. <https://doi.org/10.1007/s11214-020-00787-3>
- Quémerais, E., Chaufray, J. Y., Koutroumpa, D., Leblanc, F., Reberac, A., Lustrent, B., et al. (2020). PHEBUS on Bepi-Colombo: Post-launch update and instrument performance. *Space Science Reviews*, 216(4), 67. <https://doi.org/10.1007/s11214-020-00695-6>
- Schlemm, C. E., Starr, R. D., Ho, G. C., Bechtold, K. E., Hamilton, S. A., Boldt, J. D., et al. (2007). The X-Ray spectrometer on the MESSENGER spacecraft. *Space Science Reviews*, 131, 393–415. <https://doi.org/10.1007/s11214-007-9248-5>
- Schrifer, D., Trávníček, P., Ashour-Abdalla, M., Richard, R. L., Hellinger, P., Slavin, J. A., et al. (2011b). Electron transport and precipitation at Mercury during the MESSENGER flybys: Implications for electron-stimulated desorption. *Planetary and Space Science*, 59, 2026–2036. <https://doi.org/10.1016/j.pss.2011.03.008>
- Schrifer, D., Trávníček, P. M., Anderson, B. J., Ashour-Abdalla, M., Baker, D. N., Benna, M., et al. (2011a). Quasi-trapped ion and electron populations at Mercury. *Geophysical Research Letters*, 38. <https://doi.org/10.1029/2011GL049629>
- Simpson, J. A., Eraker, J. H., Lampert, J. E., & Walpole, P. H. (1974). Electrons and protons accelerated in Mercury's magnetic field. *Science*, 185(4146), 160–166. <https://doi.org/10.1126/science.185.4146.160>
- Slavin, J. A., Acuña, M. H., Anderson, B. J., Baker, D. N., Benna, M., Gloeckler, G., et al. (2008). Mercury's magnetosphere after MESSENGER's first flyby. *Science*, 321, 85–89. <https://doi.org/10.1126/science.1159040>
- Slavin, J. A., Baker, D. N., Gershman, D. J., Ho, G. C., Imber, S. M., Krimigis, S. M., & Sundberg, T. (2018). Mercury's dynamic magnetosphere. In S. C. Solomon, L. R. Nittler, & B. J. Anderson (Eds.), *Mercury: The view after MESSENGER* (pp. 461–496). Cambridge University Press. <https://doi.org/10.1017/9781316650684.018>
- Slavin, J. A., DiBraccio, G. A., Gershman, D. J., Imber, S. M., Poh, G. K., Raines, J. M., et al. (2014). MESSENGER observations of Mercury's dayside magnetosphere under extreme solar wind conditions. *Journal of Geophysical Research: Space Physics*, 119(10), 8087–8116. <https://doi.org/10.1002/2014JA020319>
- Solomon, S. C., McNutt, R. L., Gold, R. E., & Domingue, D. L. (2007). MESSENGER mission overview. *Space Science Reviews*, 131, 3–39. <https://doi.org/10.1007/s11214-007-9247-6>
- Solomon, S. C., Nittler, L. R., & Anderson, B. J. (2018). *Mercury: The view after MESSENGER*. Cambridge University Press.
- Starr, R. D. (2010). MESSENGER E/V/H XRS calibrated (CDR) spectra v1.0. *NASA Planetary Data System*. <https://doi.org/10.17189/1518576>
- Starr, R. D., Schrifer, D., Nittler, L. R., Weider, S. Z., Byrne, P. K., Ho, G. C., et al. (2012). MESSENGER detection of electron-induced X-ray fluorescence from Mercury's surface. *Journal of Geophysical Research*, 117, E00L02. <https://doi.org/10.1029/2012JE004118>
- Walsh, B. M., Ryou, A. S., Sibeck, D. G., & Alexeev, I. I. (2014). Energetic particle dynamics in Mercury's magnetosphere. *Journal of Geophysical Research Space Physics*, 118, 1992–1999. <https://doi.org/10.1002/jgra.50266>

- Weider, S. Z., Nittler, L. R., Starr, R. D., Crapster-Pregont, E. J., Peplowski, P. N., Denevi, B. W., et al. (2015). Evidence for geochemical terranes on Mercury: Global mapping of major elements with MESSENGER's X-Ray Spectrometer. *Earth and Planetary Science Letters*, 416(0), 109–120. <https://doi.org/10.1016/j.epsl.2015.01.023>
- Yoshikawa, I., Korablev, O., Kameda, S., Rees, D., Nozawa, H., Okano, S., et al. (2010). The Mercury sodium atmospheric spectral imager for the MMO spacecraft of Bepi-Colombo. *Planetary and Space Science*, 58(1), 224–237. <https://doi.org/10.1016/j.pss.2008.07.008>